Echo trains in pulsed electron spin resonance of a strongly coupled spin ensemble – Supplemental Material

Stefan Weichselbaumer,[1,2] Matthias Zens,[3,4] Christoph W. Zollitsch,[1,2,*]
Martin S. Brandt,[5,2,6] Stefan Rotter,[3] Rudolf Gross,[1,2,6] and Hans Huebl[1,2,6,†]

[1] *Walther-Meißner-Institut, Bayerische Akademie der Wissenschaften, 85748 Garching, Germany*
[2] *Physik-Department, Technische Universität München, 85748 Garching, Germany*
[3] *Institute for Theoretical Physics, TU Wien, Wiedner Hauptstraße 8-10/136, 1040 Vienna, Austria*
[4] *ITAMP, Harvard-Smithsonian Center for Astrophysics, Cambridge, Massachusetts 02138, USA*
[5] *Walter Schottky Institut, Technische Universität München, 85748 Garching, Germany*
[6] *Munich Center for Quantum Science and Technology (MCQST), Schellingstraße 4, 80799 München, Germany*

(Dated: July 15, 2020)

I. EFFECT OF PULSE IMPERFECTIONS AND COUPLING STRENGTH

Fully avoiding pulse errors in an inhomogeneously broadened spin ensemble is a challenging task that depends on the distribution of coupling strengths and spin frequencies as well as on the experimental circumstances. In particular, pulses of finite lengths and simple shapes typically result in imperfect rotation angles of individual spins in the experiment. However, as outlined in the main text, rotation errors are also proving to be an important part of the multi-echo formation process.

To determine the impact of rotation errors we present here additional simulations, where the action of the two microwave pulses in the Hahn echo sequence is included in the initial conditions of our theoretical model. The purpose of this procedure is to disentangle the intricate strong coupling dynamics during the $\pi/2$- and π-pulses from the subsequent dynamics. To be specific, we solve the Maxwell-Bloch equations for the initial conditions $\langle a\rangle = 0$, $\langle\sigma_j^x\rangle = -\cos(\Delta_j\tau)\cos(\alpha)$, $\langle\sigma_j^y\rangle = -\sin(\Delta_j\tau)$, and $\langle\sigma_j^z\rangle = \cos(\Delta_j\tau)\sin(\alpha)$ at $t = 0$, where $\Delta_j = \omega_j - \omega_p$ is the detuning between the spin frequency and the reference rotating frame, $\tau = 20\,\mu$s is now the inter pulse delay, and α is the rotation angle of the second pulse. Note that these specific initial conditions correspond to a situation where all spins are collectively brought into the xy-plane using a perfect $\pi/2$-rotation along the y-axis for the first pulse. Then, after a free evolution time τ, the spin ensemble is artificially rotated by an angle α along the y-axis. Note that with this procedure we effectively switch off the collective coupling between the spin ensemble and the resonator during this entire preparation period. As a result, we can study the impact of the spin-resonator coupling and rotation errors independently of the imperfections imposed by the microwave pulses.

In Fig. S1 we present the results for the average spin expectation values $S_{\mathrm{av}}^{x,z} = \sum_j\langle\sigma_j^{x,z}\rangle/N$ for a Gaussian spin distribution, where we distinguish two different settings: (i) We consider a strongly coupled spin ensemble ($g_{\mathrm{eff}}/2\pi = 1.56\,$MHz) and compare the evolution involving a perfect ($\alpha = \pi$) and a slightly imperfect ($\alpha = 0.95\pi$) refocusing pulse. (ii) We compare the dynamic evolution involving an imperfect rotation ($\alpha = 0.95\pi$) for strong ($g_{\mathrm{eff}}/2\pi = 1.56\,$MHz) and very weak ($g_{\mathrm{eff}}/2\pi = 1.56\,$kHz) coupling to the resonator. We first note, that the conventional Hahn echo at $t = 20\,\mu$s is observed in S_{av}^x, regardless of both the coupling strength and the rotation error. Next, we compare the impact of the pulse rotation angle under strong coupling. While the results for the perfect and the imperfect rotation almost overlap during the conventional Hahn echo, additional echos at $t = 40\,\mu$s and $t = 60\,\mu$s arise only for $\alpha = 0.95\pi$, indicating that the pulse imperfections are relevant for the multi-echo formation. Staying with $\alpha = 0.95\pi$, but reducing the coupling strength to $g_{\mathrm{eff}}/2\pi = 1.56\,$kHz reveals the key role of the spin-resonator coupling. Although the spins build up a large dipole moment S_{av}^x during the conventional Hahn echo, the coupling to the resonator is too weak to cause a significant rotation of the spins on the Bloch sphere and therefore no visible echos are produced at later times. Our findings thus suggest that the enhanced rotation of the spins during the echos in combination with an imperfect refocusing pulse are the key building blocks for the formation of multiple echos.

II. VARIATION OF THE PULSE DELAY TIME τ

One key parameter in the Hahn echo sequence is the inter-pulse delay τ, which is varied in experiments to determine the coherence time of the spin ensemble. In particular, the analysis of the decay of the conventional Hahn echo gives access to this characteristic time. In this spirit, we present in Fig. S2 the experimentally determined echo areas as a function of their arrival time for various τ recorded at a fixed magnetic feld of 170.18 mT using a wait time of 180 s between measurements. We find for the experimental data that the subsequent echos show a decreasing amplitude, which can be well described by an exponential decay (lines in Fig. S2 (a)). The corresponding characteristic decay times T_{decay} increase for

* Present address: London Centre for Nanotechnology, University College London, London WC1H 0AH, United Kingdom
† hans.huebl@wmi.badw.de

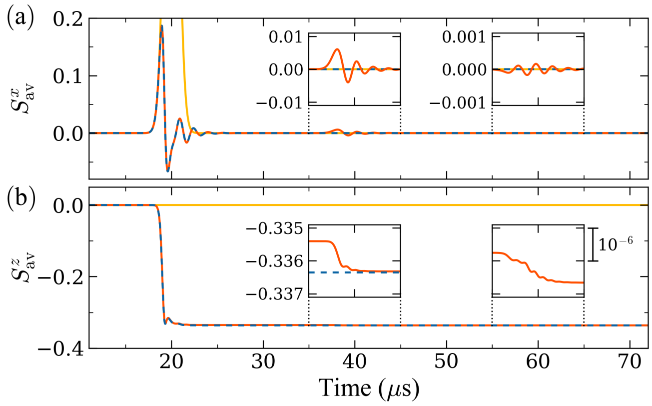

Figure S1. Average spin expectation values $S^{x,z}_{\mathrm{av}} = \sum_j \langle \sigma^{x,z}_j \rangle / N$ versus time for a spin ensemble starting from an initial condition that imitates a Hahn echo sequence of a perfect $\pi/2$-rotation followed by an α-rotation right before $t = 0$. (a) S^x_{av} for a strongly coupled spin ensemble, $\Omega/2\pi = 1.56\,\mathrm{MHz}$, after a perfect rotation $\alpha = \pi$ (blue dashed) and an imperfect rotation $\alpha = 0.95 \times \pi$ (red). The imperfect rotation $\alpha = 0.95\pi$ is also shown for weak coupling $\Omega/2\pi = 1.56\,\mathrm{kHz}$ (yellow). The conventional Hahn echo at $t = 20\,\mu\mathrm{s}$ is present in all situations, while additional echos at $t = 40\,\mu\mathrm{s}$ and $t = 60\,\mu\mathrm{s}$ (insets) are visible only for the combination of imperfect rotations and strong coupling. (b) Due to the strong coupling (blue and red) S^z_{av} changes significantly during the conventional Hahn echo. This effective rotation of the spin ensemble is absent for weak coupling (yellow). Much smaller but similar rotations are visible at $t = 40\,\mu\mathrm{s}$ and $t = 60\,\mu\mathrm{s}$ (insets) for $\alpha = 0.95\pi$ (red), but not for $\alpha = \pi$ (blue). (Also in the right inset, the blue dashed line shows no variation, but falls outside of the zoom window.)

longer inter-pulse delays τ. This can be rationalized by the observation that the formation of an echo constitutes an effective decay channel. Thus, we expect that T_{decay} should be fundamentally limited by the coherence time T_2, which is the case for the data presented here. In addition, we can compare the experimental observations with our theoretical model. In particular, we choose a Lorentzian and a Gaussian spin distribution of the same width γ_s to study their impact on the echo decay. For both spin distributions the amplitude of the driving is chosen such that the first pulse corresponds to an effective $\pi/2$-rotation. On a first glance, we find that both spin distributions corroborate the experimental data, as both predict an initial exponential decay. However, we also find characteristic differences in the decay. For instance, while the Gaussian-shaped distribution can be well described by an exponential decay, the Lorentzian-shaped distribution initially falls off with a fast rate and decays at later times with a noticeably smaller rate. On a quantitative level, the initial decay rates observed in the experiment are in reasonable agreement with the initial decay rates of the Lorentzian-shaped spin distribution (maximum deviation of 20%). For the Gaussian spin distribution the decay times of the individual echo trains exceed those observed in the experiment by approximately

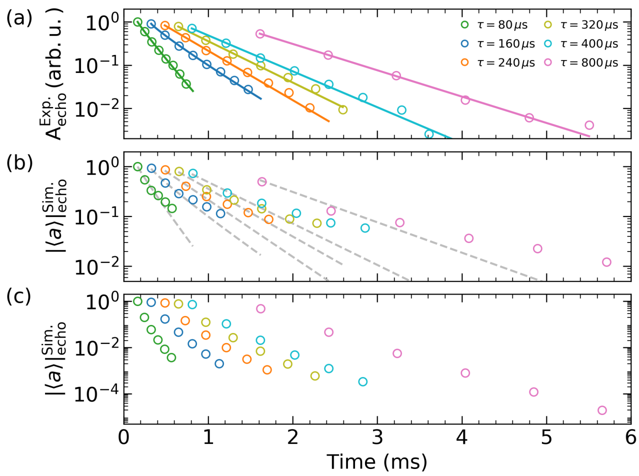

Figure S2. (a) Experimental data: Integrated echo area for the individual echos as a function of time, shown for several echo spacings τ. Solid lines are fits to an exponential decay law. (b,c) Simulation: Maxima of the individual echos as a function of time, shown for several echo spacings τ assuming (b) a Lorentzian and (c) a Gaussian spin distribution. For comparison we show the fits to the experimental data again in (b) (gray dashed lines). All data points are normalized to the area/hight of the first echo of the $\tau = 80\,\mu\mathrm{s}$ dataset.

a factor of 10. In general, we note that the decay of the echo train does not only depend on τ and the characteristic parameters of the system, such as κ, κ_{ext}, γ_{s}, but also strongly depends on the exact shape of the spin distribution. In addition, we suspect that the dipole-dipole interaction present within the spin ensemble could additionally affect the characteristic decay time and speculate that the details of the experiment such as the spatial distribution of the excitation field B_1 as well as the amplitude and temporal shape the microwave pulses have the potential to modify this decay. A detailed analysis of these dependencies will be the subject of future work.

III. EXPERIMENTAL SETUP

Below, we describe in detail the experimental setup used to obtain the results presented in the main text. We first describe the sample preparation, followed by a description of the cryogenic and room-temperature microwave circuitry. The sub-section III C describes the digital down-conversion of the signal after digitization. Finally, we describe how we determine the integration window for the echo area integration of the echo trains.

A. Sample preparation

The sample investigated in the main part consists of two parts: a superconducting planar microwave resonator and a paramagnetic electron spin ensemble.

The microwave resonator is fabricated on top of a $6 \times 10\,\mathrm{mm}^2$ high-resistivity ($> 10\,\mathrm{k\Omega cm}$) silicon substrate with natural isotope composition. The substrate is first cleaned in an ultrasonic bath using acetone and isopropyl alcohol. Then, a 150 nm thick niobium layer is deposited onto the substrate in a sputter process. Next, the chip is spin-coated with photo resist and the resonator structure is defined via optical lithography. After development, the structure is transferred into the superconducting film using a reactive ion etching process. The chip is then placed into a gold-plated (oxygen-free highly-conductive) copper box and connected to this enclosure using conductive silver-glue at its boundaries. This forms the ground connection of the resonator. SMA end launch connectors are then inserted from both ends and the center pin of the end-launch is connected to the coplanar waveguide using silver glue.

As paramagnetic electron spin ensemble, we use phosphorus donors with a doping concentration of $[P] = 1 \times 10^{17}\,\mathrm{cm}^{-3}$ embedded in an isotopically purified ^{28}Si host crystal with a residual ^{29}Si concentration of 0.1 %. The ^{28}Si:P crystal has a thickness of 20 µm and was originally grown on top of a heavily boron-doped $^{\mathrm{nat}}$Si substrate. An additional 500 nm thick arsenic doped $^{\mathrm{nat}}$Si layer was grown on top of the ^{28}Si:P layer. We remove these additional layers by a combination of mechanical polishing and reactive ion etching. The resulting 20 µm thick flakes are then placed with the utmost care on top of the resonator. The flakes are pressed onto the resonator using an additional piece of an $^{\mathrm{nat}}$Si wafer and a PTFE screw in the lid of the sample box.

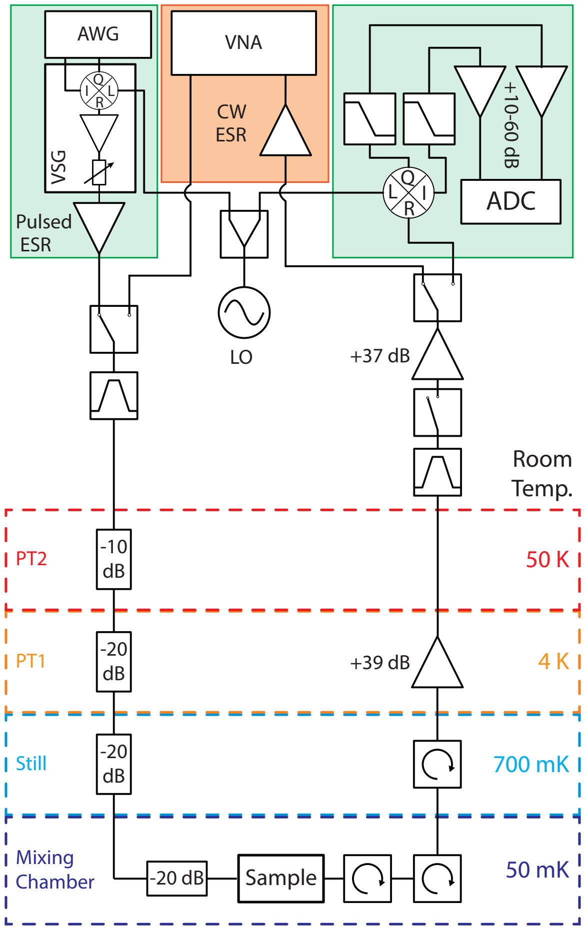

Figure S3. Microwave setup for continuous-wave (red) and pulsed (green) electron spin resonance experiments. Details of the pulse bridge and detection scheme are given in the text.

B. Microwave circuit

The microwave circuitry used in this work is presented in Figure S3.

The main goal of the cryogenic microwave circuitry is to suppress room temperature noise photons from reaching the sample under investigation. To this end, the input lines are attenuated by 70 dB at the various temperature stages. On the output side, we use two cryogenic circulators on the mixing chamber stage as well as one at the still level. The outgoing signal is amplified by a cryogenic HEMT amplifier (Low Noise Factory LNC4_8A) at the 4K stage.

The microwave circuitry at room temperature to perform both continuous-wave (CW) as well as pulsed ESR measurement via two latching electromechanical RF switches (Keysight 8765B). The signal entering the cryostat is bandpass-filtered (MiniCircuits VBFZ-5500-S+) to the relevant frequency range to reduce the power load on the subsequent cryogenic stages. The output signal is bandpass-filtered as well before entering a fast PIN diode switch (Analog Devices HMC-C019). This switch blanks out the high-power microwave pulses from entering the sensitive down-conversion setup. The signal is then further amplified at room-temperature (B&Z Technology BZP110UC1).

To perform CW ESR measurements, we connect a vector network analyzer (Rhode & Schwarz ZVA8) to the input and output line and measure the transmission scattering parameter $|S_{21}|^2$.

Pulsed ESR measurements are performed using a inhouse built microwave bridge. We generate in-phase and quadrature signals of Gaussian-shaped pulses using a fast arbitrary waveform generator (Agilent M8190A, 12 GS/s) at an intermediate frequency of $f_{\mathrm{IF}} = 42.5\,\mathrm{MHz}$. The pulses are then up-converted to the resonance frequency using a vector signal generator (Rhode & Schwarz SGS100A) and further amplified (CTT AGX0218-3964) before reaching the input side of the cryostat. The pulse power before the microwave switch at the input of the cryostat is +25 dBm, resulting in a maximum echo signal for pulse times of 1 µs and 2 µs.

Detection of the resulting spin echos is performed by a heterodyne down-conversion setup. The signal is down-converted using an IQ mixer (Marki IQ-0307L). The down-converted signal with frequency f_{IF} is then lowpass-filtered to reduce LO leakage. The signal is amplified with variable gain between 10 and 60 dB (FEMTO DHPVA-200) to utilize the full dynamic range of the analog-to-digital converter (Spectrum M4i.4451-x8). The digitizer card records both the in-phase and quadrature component at a sample rate of 500 MS/s.

To ensure a stable phase synchronization between the devices, all devices are synchronized using an oven-stabilized 10 MHz reference signal (Stanford Research Systems FS725). The LO signal (Agilent E8257D) is provided to both the vector network source as well as the IQ mixer using a power divider.

C. Signal demodulation

In this section we describe our algorithm to demodulate the signal at the intermediate frequency (here $f_{\mathrm{IF}} = 42.5\,\mathrm{MHz}$) to baseband (DC). We first calculate the complex signal $Z = I(t) + iQ(t)$ from the recorded in-phase and quadrature signal. The microwave transmission signal S_{21} is obtained by multiplying Z with a complex sinusoidal

$$S_{21} = Z \cdot \exp\left(-i\left(2\pi f_{\mathrm{IF}} + \phi\right)\right), \tag{S1}$$

where f_{IF} is the intermediate frequency and ϕ is the demodulation phase. This shifts the frequency of the signal to the baseband. We choose ϕ in such a way that the signal in the real part of S_{21} is maximized. After the frequency conversion, we apply a lowpass filter (digital Butterworth filter of 5th order) with a cutoff frequency of 10 MHz and re-sample the signal at a sample rate of 20 MS/s to reduce the file size of the measured signals.

D. Echo integration

In the following we describe our procedure to integrate the echo signal. The key here is to determine the length of the integration window, Δt, given the following two challenges:

1. For short τ, we cannot use a very broad integration window, as the echo peaks are close to each other. Therefore, the integration window has to be chosen for each value of τ individually.

2. As we integrate the magnitude of the signal $|S_{21}|$, there is a finite DC offset V_{offset} present in the signal. This offset adds a finite contribution $V_{\mathrm{DC}} \cdot \Delta t$ to the integrated echo area, where Δt is the length of the integration window.

Our algorithm works as follows: First, we determine all echo peaks using a peak-detection algorithm. In the next step, we integrate the signal using a numerical trapezoid integration, centered around the second detected echo peak with varying integration window Δt. When plotting

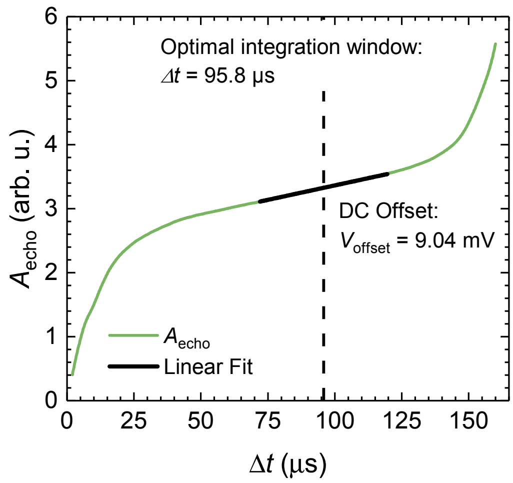

Figure S4. Determining the integration window Δt and DC offset V_{offset}. For details see text.

A_{echo} as a function of Δt, we can distinguish three regions (c.f. Figure S4):

A steep increase for small (large) values of Δt. These are caused by partial integration of the investigated (next) echo peak. In the intermediate region, we observe a linear increase of A_{echo} with Δt. Here, the investigated echo peak is completely inside the integration window and the increase of the echo area is due to the integration of the DC offset. To determine the optimal integration window, we calculate the minimum of the first derivative $\mathrm{d}A_{\mathrm{echo}}/\mathrm{d}\Delta t$ (dashed line in Figure S4). The DC offset is determined as the slope of a linear fit in the linear regime (solid line in Figure S4).

For the final integration, we subtract the DC offset from the magnitude signal and integrate each detected echo peak using the previously determined integration window.

IV. SPIN-RESONATOR COUPLING

In this section, we discuss the spin-resonator coupling. The planar resonator structure used in our experiments creates an inhomogenous microwave magnetic field and leads therefore to a distribution of the spin-resonator coupling rate. The analysis of the coupling rate in the presence of an inhomogeneous microwave magnetic field distribution is based on our work described in Ref. [R1].

A schematic of the resonator used in the experiment is displayed Fig. S5 (a). The resonator is embedded in the ground plane of a coplanar waveguide (signal line width $w = 20\,\mu\mathrm{m}$, gap width $s = 12\,\mu\mathrm{m}$). The resonator is separated from the signal line by a screening line (width $w_{\mathrm{gs}} = 10\,\mu\mathrm{m}$), which defines the external coupling rate [R1]. The resonator consists of an inductor (wire width $w_{\mathrm{i}} = 5\,\mu\mathrm{m}$, pitch distance $p = 20\,\mu\mathrm{m}$) with a total length of $l_{\mathrm{ind}} = 11.35\,\mathrm{mm}$ and a finger capacitor.

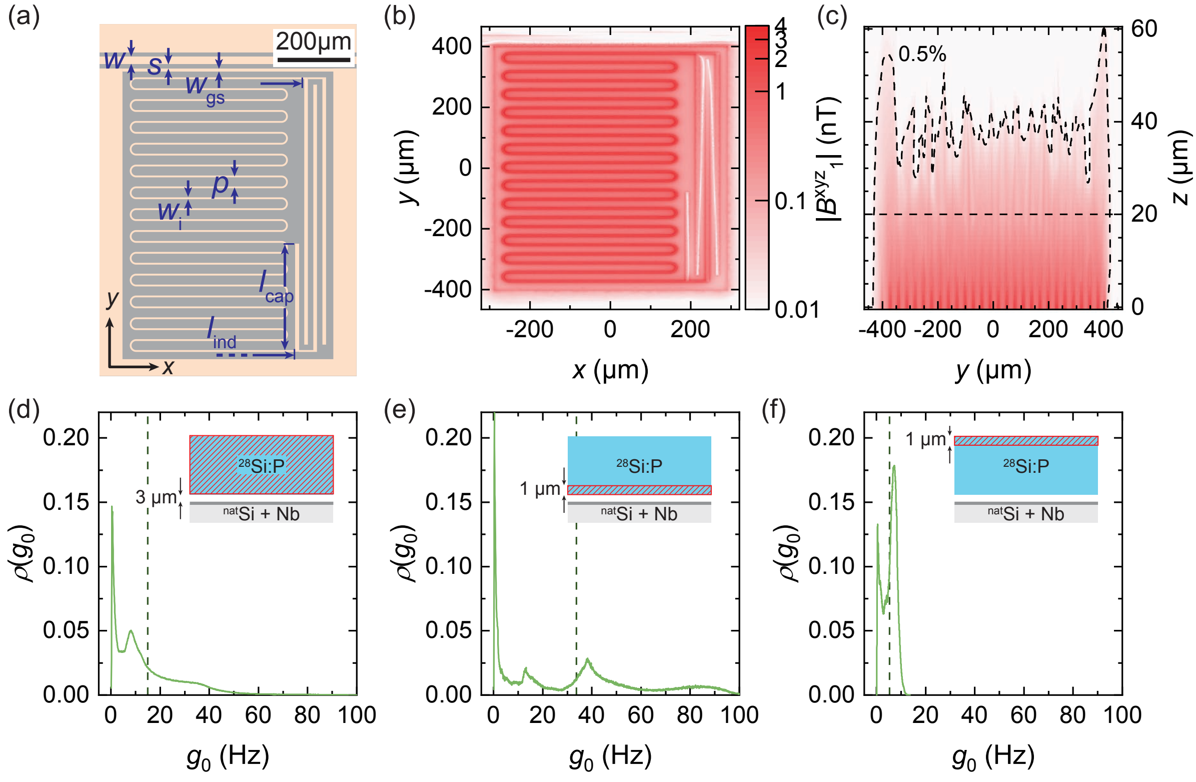

Figure S5. Analysis of the resonator used in the experiment. (a) Schematic of the lumped element resonator. (b) Field distribution in a top-view. (c) Field distribution in the yz-plane for $x = 0$. The dashed line indicates the region where the amplitude decayed to 0.5 % of the maximum amplitude. (d)-(f) Distribution of the collective coupling rate for (d) $0 < z \leq 20\,\mu$m, (e) $0 < z \leq 1\,\mu$m and (f) $19\,\mu\text{m} < z \leq 20\,\mu$m. The dashed line indicates the average coupling strength in this sample region.

By changing the length l_{cap} of the capacitor finger the resonance frequency can be tuned.

For a further analysis, we perform finite element simulations using CST Microwave Studio 2016 [R2] to extract the three-dimensional microwave magnetic field distributions of the resonator. Figures S5 (b) and (c) show the spatial distribution of the magnitude of the vacuum magnetic field fluctuations $|B_1^{yz}|$, i.e. the field component that is perpendicular to the static magnetic field B_0 along the x-direction. The data is exported from CST Microwave Studio in volume elements of $1 \times 1 \times 1\,\mu\text{m}^3$. The dashed line in panel (c) marks the region where the field amplitude decayed to 0.5 % of the maximum field amplitude. We define this volume as the mode volume of the resonator $V_{\text{m}} = 1.41 \times 10^{-11}\,\text{m}^3$. Due to the anti-parallel current flow in the inductor wires, the dynamic magnetic field interferes destructively in the far-field. This limits how far the magnetic field reaches into the z-direction and enhances the sensitivity of the resonator to spins close to the superconducting resonator.

The single spin-resonator coupling is given by [R3]

$$g_0 = g_{\text{s}}\mu_{\text{B}}B_{1,0}/\hbar, \tag{S2}$$

where $g_{\text{s}} = 1.9985$ is the electron g-factor of phosphorus donors in silicon [R4] and μ_{B} is the Bohr magneton. $B_{1,0}$ describes the magnetic field generated by vacuum fluctuations in the resonator. $B_{1,0}$ is given by [R5] $B_{1,0} = \sqrt{\mu_0\hbar\omega_r/(2V_{\text{m}})}$, where μ_0 is the vacuum permeability, $\hbar$ is the reduced Planck constant and ω_r is the resonance frequency of the resonator. Collective coupling effects lead to an enhancement of the single-spin coupling rate by a factor $\sqrt{N}$, where N is the number of spins. Thus, the collective coupling strength is given as

$$g_{\text{eff}} = \frac{g_{\text{s}}\mu_{\text{B}}}{2\hbar}\sqrt{\frac{1}{2}\mu_0\hbar\omega_{\text{r}}\rho_{\text{eff}}\nu}. \tag{S3}$$

In this expression, the number of spins, N, is replaced by $N = \rho_{\text{eff}}V = \rho P(T)V$, where ρ is the donor concentration, $P(T)$ is the thermal spin polarization and V is the sample volume. The filling factor $\nu = V/V_{\text{m}}$ describes the ratio between the sample volume and the mode volume of the resonator.

The planar resonator structures used in this experiment generate an inhomogeneous microwave magnetic field B_1, which has to be taken into account in the filling factor

$$\nu = \frac{\int_{\text{Sample}} B_1^2(\vec{r})\,\text{dV}}{\int_{\text{Mode}} B_1^2(\vec{r})\,\text{dV}}. \tag{S4}$$

We can calculate the filling factor from the exported three-dimensional distribution of the microwave magnetic field using the expression

$$\nu = \frac{\sum_V \left| B_{1,\mathrm{sim}}^{yz}(\vec{r}) \right|^2}{\sum_{V_\mathrm{m}} \left| B_{1,\mathrm{sim}}^{xyz}(\vec{r}) \right|^2}. \tag{S5}$$

With this approach, we obtain a theoretically expected spin-resonator coupling of 2.33 MHz, which somewhat over-estimates our experimentally defined value. We explain this by a small gap between the resonator and the spin sample [R6]. Assuming a gap of (2.91 ± 0.02) µm, we obtain a quantitative agreement between the theoretically expected spin-resonator coupling and the experimentally determined value of 1.54 MHz. However, we want to emphasize, that one ingredient for the observation of the phenomenon of a self stimulated echo train is a sufficiently large coupling rate g_eff, i.e. placing the system in the strong coupling regime.

Using Eq. S2 we can calculate the distribution of the single spin-resonator coupling g_0. We present the data in Fig. S5 (d) to (f) for different regions above the resonator. Note that we included the finite gap between the resonator and the sample in these calculations. Panel (d) presents the coupling distribution over the entire sample region with a mean coupling strength of $g_{0,\mathrm{mean}} = 14.93$ Hz (dashed line). This results in a number of spins contributing to the signal according to $N \approx (g_\mathrm{eff}/g_{0,\mathrm{mean}})^2 = 1.06 \times 10^{10}$. For a thin layer of the spin ensemble facing the resonator we compute an enhanced single spin-resonator coupling strength with a mean value of 33.74 Hz, while spins on the opposite side (panel (f)) couple relatively weakly with on average 5.33 Hz. The low-frequency peak in the coupling distribution can be attributed to spins outside the resonator dimensions, at the edges of the sample.

V. ESTIMATE OF THE DRIVEN RABI FREQUENCIES AND PULSE LENGTHS

The finite element simulation of the microwave resonator also allows us to estimate the microwave B_1 fields present during the microwave pulses and correspondingly the expected pulse durations for the $\pi/2$ and π pulses. In a simplifying estimate, we can utilize the computed g_0 from Fig. S5 to estimate the driven Rabi frequency ω_1, as the latter is given by $g_0\sqrt{n_\mathrm{c}}$ (cf. Eq. S2) [R1, R7, R8]. For an initial estimate for n_c, we turn to the Maxwell-Bloch equations and in particular (S13). In detail, we relate the driving amplitude $\eta = \sqrt{\frac{2\kappa_\mathrm{ext} P_\mathrm{mw}}{\hbar\omega_\mathrm{c}}}$ to the experimental microwave power P_mw. For a coarse estimate, we further assume a resonant excitation of the microwave resonator with the external microwave tone ($\Delta_\mathrm{c} = 0$) and neglect the modifications of the microwave susceptibility of the system stemming from the strong coupling between the spin ensemble to microwave radiation. Note, that these reduce the photon number n_c in a complex fashion, and hence we expect to overestimate our driven Rabi frequency. Using the parameters given in the main text, we find $n_\mathrm{c} = 2.1 \times 10^{10}$ for a peak microwave power of +25dBm at the input of the dilution refrigerator, where we assume that attenuation is solely given by the microwave attenuators presented in Fig. S3 (a total of 70dB attenuation).

In the driven Rabi regime, we next quantitatively estimate ω_1 by $g_0\sqrt{n_\mathrm{c}}$. Using the peak in Fig. S5 (d) at $g_0/2\pi = 8$ Hz, we obtain $\omega_1/2\pi = 1.2$ MHz corresponding to a $\pi/2$-time of 200 ns. This is a factor of 5 shorter than our experimentally chosen $\pi/2$ time, however it is worth to point out that this estimate is purely based on the design parameters of the resonator and the attenuators mounted in microwave delivery lines in the setup. Hence, this estimate neglects the additional input losses of the microwave lines, the insertion-loss of the microwave switch and the band pass filter as well as cable connectors, all of which are part of the microwave input circuitry. Those will further reduce the input power supplied to the resonator (we estimate this to be of the order of 5-10dB, corresponding to a reduction in ω_1 between a factor of roughly 2-3). In addition, this estimate also neglects the modified transmission when the spin ensemble is set in resonance with the microwave resonator. In summary, our crude estimate for the pulse durations for a $\pi/2$ and π pulse agrees well with our selected pulse times. Moreover, this estimate also emphasizes that the pulses have a significant B_1 distribution as can be seen in Fig. S5 d).

VI. EXPERIMENTAL PULSE OPTIMIZATION

Experimentally, we optimize the pulse angles via the detected echo amplitude. In detail, we vary the pulse length of the first pulse t_duration and second pulse $2 \cdot t_\mathrm{duration}$ until we observe a maximum in the echo amplitude. Although this analysis does not give direct information about the pulse angles of the first and second pulse, we experimentally notice that our pulse settings allow for a partial inversion of the echo, as seen in Sec. IX. This observation suggests that we indeed obtain a rotation angle of the order of 180° for our effective π-pulse and hence confirms the rotation angles of the order of 90° for our effective $\pi/2$-pulse.

VII. PHASE CYCLING EXPERIMENTS

The experimental data in the main text were recorded with a "$+x/+x$" pulse sequence, i.e. the two microwave pulses are in phase. We have additionally recorded echo trains where a relative phase shift between the two pulses has been applied. In order to verify the occurence of the echo train phenomenon, a second sample has been used,

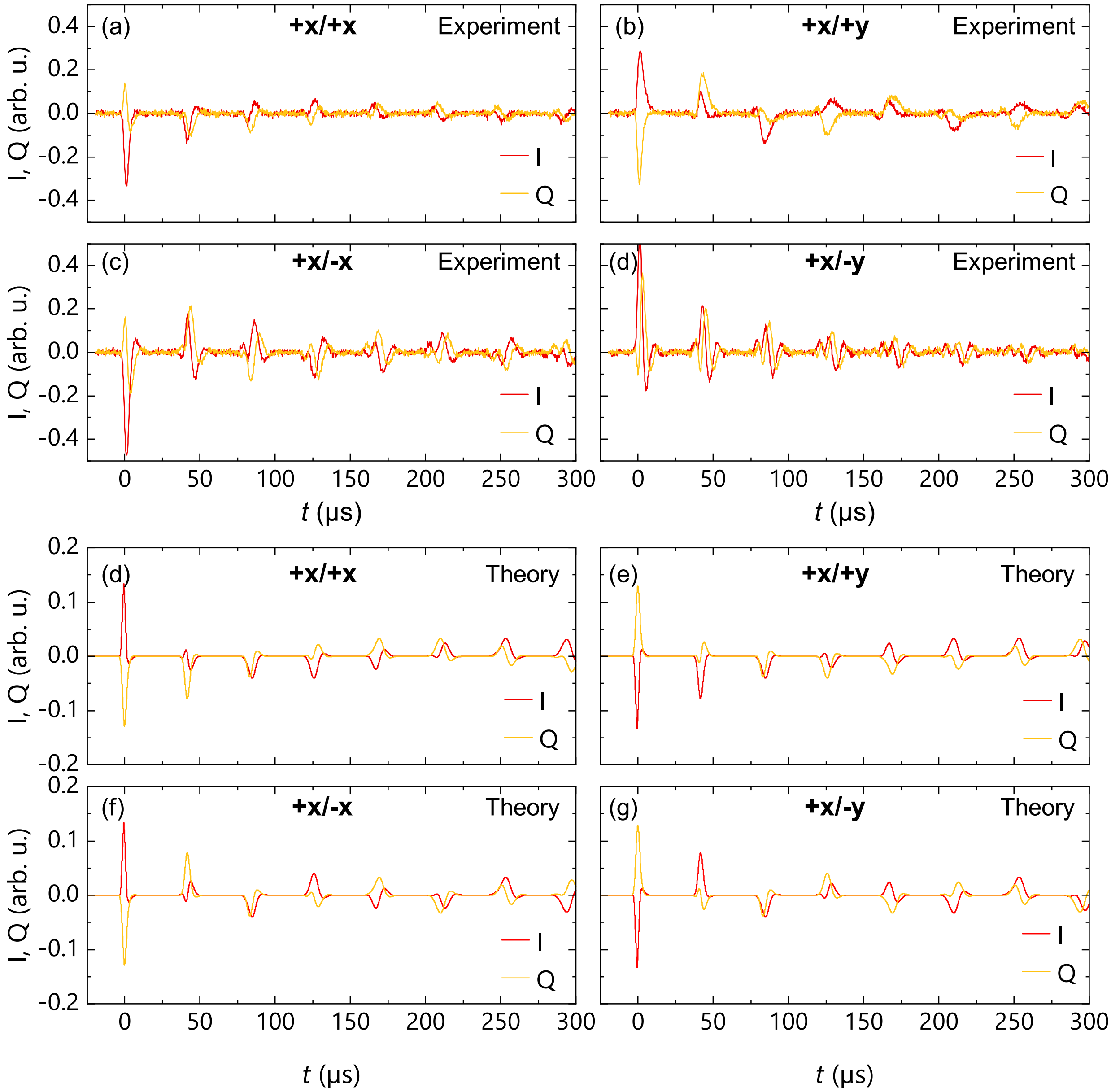

Figure S6. Phase cycling measurements. Quadratures I and Q of the recorded and simulated microwave transmission for (a), (e) $+x/+x$, (b), (e) $+x/+y$ (90° phase shift), (c), (f) $+x/-x$ (180° phase shift) and (d), (g) $+x/-y$ (270° phase shift). The magnetic field was set to the low-field hyperfine transition, which is strongly coupled to the microwave resonator. The echo signal is contained in both microwave signal quadratures and no clear phase relation between subsequent echos is visible.

which is nominally identical to the sample used in the main text. The experiments were performed with the magnetic field centered on the low-field hyperfine transition of the phosphorus donors, which is strongly coupled to the microwave resonator. In Fig. S6, we show the recorded quadratures, I and Q of the microwave transmission signal as a function of time for (a) $+x/+x$, (b) $+x/+y$ (90° phase shift), (c) $+x/-x$ (180° phase shift and (d) $+x/-y$ (270° phase shift). In contrast to conventional ESR experiments, where the ESR signal is typically contained in a single phase, in the strong coupling regime the microwave signal is contained in both quadratures. Additionally, no clear phase relation between subsequent echos is observable but rather a phase rotation from one echo to the next. We plot the quadratures of the simulated microwave transmission signal for $+x/+x$ and $+x/+y$ in panel (e) and (f), respectively. Our simulations can qualitatively reproduce the complicated phase relation of the echos.

VIII. CONVENTIONAL T_2 MEASUREMENTS

In a conventional ESR experiment, the coherence time T_2 is measured by Hahn echo spectroscopy. A series of Hahn echo pulse sequences consisting of two pulses are performed, where the pulse spacing τ is varied. The resulting echo appearing τ after the refocussing pulse is digitized and integrated. The echo area A_{echo} then decreases with the characteristic coherence time T_2 in an exponential fashion. We use this experimental approach to determine the coherence time T_2.

In Figure S7, we show such conventional T_2 measurements of the spin ensembles in our sample. Panel (a) shows the integrated echo area of the first (conventional) echo of the data presented in Fig. S2 (a). The exponential fit (solid line) results in $T_{2,\mathrm{conv.}} = (2.37 \pm 0.08)\,\mathrm{ms}$. As this fit contains only a small number of points due to the limited τ resolution, we have performed an additional measurement for increased τ, where we have only digitized the first echo. The evaluation of the T_2 time for this measurement presented in panel (b) results in $T_{2,\mathrm{add.}} = (2.46 \pm 0.05)\,\mathrm{ms}$, which is in agreement with the first measurement. In panel (c), we present the same measurement as in (b), with the magnetic field set to the resonance field of the P_2 dimer transition. Here, we extract a coherence time $T_{2,P_2} = (4.67 \pm 0.13)\,\mathrm{ms}$. Panel (d) shows the coherence time measurement of the $\mathrm{P_{b0}/P_{b1}}$ defects with $T_{2,\mathrm{P_{b0}/P_{b1}}} = (22.6 \pm 1.6)\,\mu\mathrm{s}$.

In samples with a large donor concentration as in our case, it is expected that the T_2 time is limited by instantaneous diffusion, originating from a dipole-dipole interaction between neighboring spins [R9, R10]. The influence of instantaneous diffusion on the T_2 time can be reduced by reducing the flipping angle of the second pulse in the Hahn echo [R10, R11]. We performed T_2 measurements and reduced the amplitude of the second pulse A_π in relation to the amplitude of the first pulse, $A_{\pi/2}$. We plot the inverse time $1/T_2$ in Fig. S8. We observe that T_2 increases when decreasing the effective flipping angle showing a maximum T_2 of 6.14 ms. The trend, that smaller rotation angles have a positive effect on T_2 is compatible with the mechanism of instantaneous diffusion. Nevertheless, one would expect that the inverse T_2 time scales with $\sin(\Theta/2)^2$, where Θ is the rotation angle of the second pulse [R12, R13]. However, Fig. S8 does not display this functional behavior, but rather a linear dependence on the pulse amplitude A_π. We speculate, that the details of the complex B_1 distribution and the spectral distribution of the spin ensemble $\rho(\omega)$ might be at the origin of this observed behavior.

The coherence times reported here are exceptionally long compared to conventional pulsed ESR experiments at higher temperatures [R10, R11]. We suspect that the long coherence times, which we find already for the initial Hahn-echo sequence, are a result of the suppression of instantaneous diffusion. As reported by Taylor et al. [R14], long and weak amplitude pulses cause an effective increase of the T_2 time by selecting only a part of the ESR transition and hereby causing a suppression of instantaneous diffusion. In a reference experiment, we performed standard measurement of the coherence time with a Hahn-echo sequence at 6 K (in a commercial Bruker ESR system) and find $T_2 \approx 30\,\mu\mathrm{s}$, which is in good agreement with e.g. Ref. [R10].

IX. T_1 MEASUREMENTS

To measure the spin life time T_1 we use an inversion recovery pulse sequence [R15], as shown in the top of Fig. S9. Conceptually, the first pulse in this three-pulse sequence inverts the spin ensemble. After a variable wait time T a standard Hahn echo with fixed τ is used to probe the magnetization along the z-axis, giving a measure of the T_1 time.

In Fig. S9 we plot the extracted echo area as a function of the wait time T for both the individual P donors and the $\mathrm{P_2}$ dimers. Note that the measurements have been recorded at an elevated temperature compared to the measurements in the main text, which, however, has only a small impact on the determined value.

For small T, the partially inverted spin ensemble has a net moment along the $-z$ axis and the resulting echo is negative. Ideally, the inversion pulse should result in a normalized echo amplitude of -1 for $T = 0$, which is not the case here, probably due to the distribution of B_1 excitation fields. With increasing T spins relax back to thermal equilibrium along $-z$ and the echo area increases. We fit the following function based on a stretched exponential to the data to extract the T_1 time:

$$A_{\mathrm{echo}} = y_0 + A \cdot \left[1 - 2\exp\left(-\left(T/T_1\right)^b\right)\right]. \tag{S6}$$

From this fit we extract $T_{1,\mathrm{P}} = (32.4 \pm 0.8)\,\mathrm{s}$ with $b = 0.75$ for the low-field hyperfine split transition. For the $\mathrm{P_2}$ dimers we extract $T_{1,\mathrm{P_2}} = (4.8 \pm 0.2)\,\mathrm{s}$ and $b = 0.43$. A stretched exponential form of the relaxation has been reported, e.g., in NMR for a superposition of single-exponential decays [R16]. As the Purcell-enhanced relaxation process depends on the spin-resonator coupling [R8], which is highly inhomogeneous in our case, we obtain a distribution of relaxation times, justifying the use of a stretched exponential. Note that we introduce an additional offset y_0 in Eq. S6 to account for non-ideal inversion due to the inhomogeneous B_1 field distribution. From the ratio $y_0/(y_0 + A) \approx 0.338$ of the phosphorus donors, we can estimate that we effectively invert about 34 % of the addressed spin ensemble.

We next discuss two mechanisms which could account for these rather short relaxation times: (i) The shortening of the T_1 time due to Purcell enhancement and (ii) the one-phonon relaxation process.

Purcell-enhanced T_1 times — One mechanism resulting in an enhanced energy relaxation time is Purcell enhancement. This mechanism is present during the free evolution time of the experiment, where each spin individually couples to the microwave resonator. Bienfait et

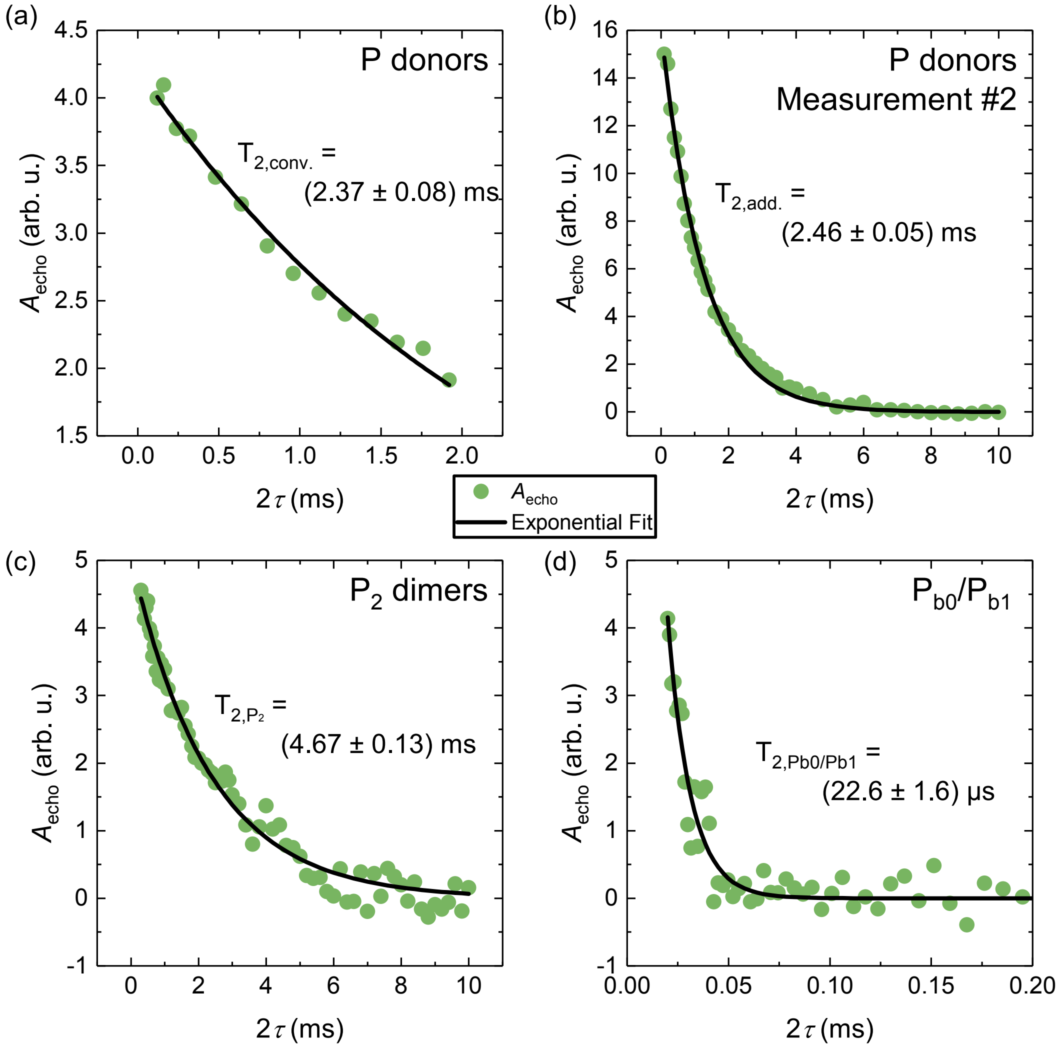

Figure S7. Determination of the coherence time T_2 using conventional Hahn echo spectroscopy for the individual donors with **(a)** the same data as presented in the main text, **(b)** data from an additional measurement, where we varied τ and only recorded the first echo, **(c)** the P_2 dimers, and (d) the $\mathrm{P_{b0}/P_{b1}}$ defects. For details see text.

al. [R8] discussed this as function of the detuning δ of the microwave resonator from the spin systems and find for bismuth donors in silicon shortened relaxation times in the seconds range. Following their discussion, we can calculate the Purcell rate by

$$\Gamma_\mathrm{P} = (2\kappa_\mathrm{c})\frac{g_0^2}{(2\kappa_\mathrm{c})^2/4+\delta}, \tag{S7}$$

where we have replaced the FWHM κ of Ref.[R8] with our HWHM κ_c. Using the peak in $g_0/(2\pi) = 8\,\mathrm{Hz}$ depicted in Fig. S5 (d) and $\kappa_\mathrm{c}/(2\pi) = 565\,\mathrm{kHz}$ of the main text, we expect a Purcell-limited T_1 time of 700 s. However, we also find a considerable amount of spins with a spin-resonator coupling of 40 Hz, which would translate to a T_1 time of 30 s. We speculate that spatial diffusion [R17–R20] can then assist with the relaxation of the majority of spins in the mode volume. However, tailored experiments, which are beyond the scope of this work, will be required to test this conjecture.

One-phonon relaxation process — In addition, we can consider the T_1 process originating from the relaxation with the phonons. As our experiments are performed

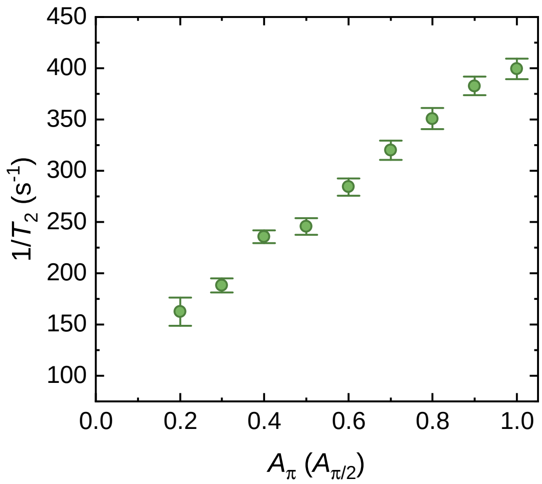

Figure S8. T_2 measurement with variable amplitude of the second pulse. By decreasing the effective flipping angle in the second pulse, instantaneous diffusion effects are reduced and T_2 increases.

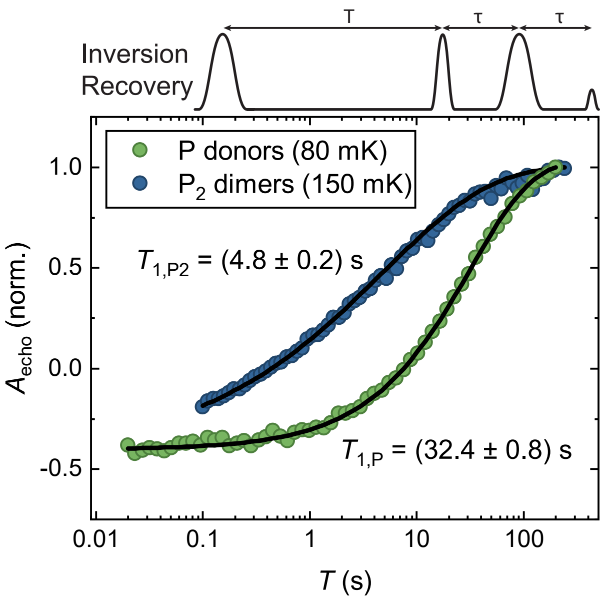

Figure S9. T_1 measurement using an inversion recovery pulse sequence (top). Due to the non-ideal inversion the curve is not symmetric to zero. The solid line is a fit to Eq. (S6).

at low temperatures, we can reduce the discussion to the one-phonon relaxation process [R21]. Morello et al. [R22] discussed this process, which was initially presented by Hasegawa et al. [R23] in the low temperature limit. Both report for $g_s\mu_B B \ll k_B T$ a temperature and magnetic field dependence of the spin lattice relaxation rate of

$$\frac{1}{T_1} \propto B^4 T. \tag{S8}$$

To discuss the phonon related relaxation process at even lower temperatures, we need to account for the phonon population, which is given by the Bose-factor $n_{\text{phonon}} = 1/(\exp(g_s\mu_\text{B}B/k_\text{B}T) - 1)$ [R23]. Then

$$\frac{1}{T_1} \propto B^5 n_{\text{phonon}} \left(1 + \exp(g_s\mu_\text{B}B/k_\text{B}T)\right) \tag{S9}$$

For $g_s\mu_\text{B}B \gg k_\text{B}T$, this simplifies to the expected B^5 dependence, while for $g_s\mu_\text{B}B \ll k_\text{B}T$ we find the limit of $T_1^{-1} \propto B^4 T$. Using the reported spin relaxation time by Feher and Gere [R21] for our donor concentration of $[P] = 1 \times 10^{17}\,\text{cm}^{-3}$ of $T_1 = 1\,\text{s}$ at $B = 0.32\,\text{T}$ as a calibration point, we can now extrapolate to our experimental temperature $T = 100\,\text{mK}$ and $B = 0.17\,\text{T}$. We find $T_1 = 110\,\text{s}$. We note that this relatively short T_1 time is mostly caused by the high doping concentration.

In summary, both presented relaxation mechanisms reasonably explain our measured spin relaxation times T_1.

In addition, we can use these estimates to calculate the expected spectral diffusion rate, which might mask the T_1 measurement and has potentially impact on the experimentally determined T_2 times presented in this paper. Spectral diffusion depends on the donor concentration [P] and the corresponding time constant is given by [R13]

$$T_{\text{SD}} = \sqrt{\frac{18\sqrt{3}}{\mu_0} \frac{\hbar}{(g_s\mu_\text{B})^2} \frac{T_1}{[P]}} \tag{S10}$$

Using the T_1 times determined above of 700 s and 110 s, we expect spectral diffusion rates of 230 ms and 91 ms, respectively. For our experimentally determined T_1 time of 32.4 s we obtain $T_{\text{SD}} = 50\,\text{ms}$. All of these estimates for T_{SD} exceed the observed T_2 times significantly and hence we expect that our T_2 measurements are not dominated by this mechanism. As the spin relaxation time represents an important parameter, we plan to investigate aspects of spin relaxation in these strongly coupled systems at a later stage in more detail using pulse sequences based on adiabatic pulses, optimal control pulses or a two-pulse saturation recovery, which have the potential to discern spectral diffusion from spin relaxation, excitation of a selected part of the spin ensemble and Purcell rates.

X. THEORETICAL MODEL

In order to give a dynamical description of the echo trains we start from the inhomogeneous Tavis-Cummings Hamiltonian [R24],

$$\begin{aligned}\mathcal{H} =& \hbar\Delta_c a^\dagger a + \frac{\hbar}{2}\sum_{j=1}^{N}\Delta_j\sigma_j^z + \sum_{j=1}^{N}\hbar[g_j\sigma_j^- a^\dagger + g_j^*\sigma_j^+ a] \\ &+ i\hbar[\eta(t)a^\dagger - \eta^*(t)a],\end{aligned} \tag{S11}$$

where $\Delta_c \equiv \omega_c - \omega_p$ and $\Delta_j \equiv \omega_j - \omega_p$ are the detunings of the resonator frequency ω_c and of the individual spin frequencies ω_j from the frequency ω_p of the incoming driving pulse. Here $a^\dagger$ and a are the creation and annihilation operators of the single resonator mode and σ_j^z, σ_j^+, and σ_j^- are the Pauli operators corresponding to the individual spins. Without loss of generality we assume $\eta^*(t) = \eta(t)$ as well as $g_j^* = g_j$. The incoming driving pulse is characterized by the carrier frequency ω_p and the amplitude $\eta(t)$, which for simplicity is assumed to be of rectangular shape. Note that the Hamiltonian (S11) does not account for direct dipole-dipole interactions between the spins. Although dipole-dipole interactions do not seem to play a fundamental role in the formation of the echo pulses it would be interesting to investigate in future studies whether they have an impact on the shape of the echos.

A quantum master equation for the system's density matrix can be written as $d\rho/dt = -\frac{i}{\hbar}[\mathcal{H}, \rho] + \mathcal{L}_D(\rho)$ [R25], where $\mathcal{H}$ is the Hamiltonian (S11) and $\mathcal{L}_D(\rho)$ stands for the standard Lindblad superoperator

$$\mathcal{L}_D(\rho) = \kappa\,(2a\rho a^\dagger - a^\dagger a\,\rho - \rho\, a^\dagger a) + \gamma_p \sum_{j=1}^{N} (\sigma_j^z \rho\, \sigma_j^z - \rho\,) + \gamma_h \sum_{j=1}^{N} (2\sigma_j^- \rho\, \sigma_j^+ - \sigma_j^+ \sigma_j^- \rho - \rho\, \sigma_j^+ \sigma_j^-). \tag{S12}$$

Here the first term describes the resonator losses with the decay rate κ and the second and third term account for nonradiative and radiative dephasing of the individual spins characterized by the rates γ_p and γ_h, respectively. Starting from the master equation given above, one can derive the equations of motion for the expectation value of any operator O by $d\langle O\rangle/dt = \mathrm{Tr}\{-\frac{i}{\hbar}[O, \mathcal{H}]\rho + O\mathcal{L}_D(\rho)\}$. In the limit of very large spin ensembles ($N \to \infty$), we can neglect correlations between the resonator field and individual spins ($\langle a^\dagger \sigma_j^-\rangle \approx \langle a^\dagger\rangle\langle\sigma_j^-\rangle$) [R26]. Thus, we obtain a closed set of first-order differential equations for the expectation values $\langle a\rangle$, $\langle\sigma_j^-\rangle$, and $\langle\sigma_j^z\rangle$, which is equivalent to the well-known Maxwell-Bloch equations:

$$\frac{d}{dt}\langle a\rangle = -(\kappa + i\,\Delta_c)\langle a\rangle - i\sum_{j=1}^{N} g_j \langle\sigma_j^-\rangle + \eta(t)\,, \tag{S13}$$

$$\frac{d}{dt}\langle\sigma_j^-\rangle = -(\gamma_\perp + i\,\Delta_j)\langle\sigma_j^-\rangle + i\,g_j\langle\sigma_j^z\rangle\langle a\rangle\,, \tag{S14}$$

$$\frac{d}{dt}\langle\sigma_j^z\rangle = -\gamma_\parallel(\langle\sigma_j^z\rangle + 1) + 2i\,g_j(\langle\sigma_j^-\rangle\langle a^\dagger\rangle - c.c.)\,, \tag{S15}$$

with the resonator decay rate κ, the longitudinal spin relaxation rate $\gamma_\parallel = 2\gamma_h = 1/T_1$, and transverse spin relaxation rate $\gamma_\perp = \gamma_h + 2\gamma_p = 1/T_2$.

As outlined in the main text, the spin ensemble is inhomogeneously broadened not only with regard to the individual spin frequencies ω_j, but also through the coupling strengths g_j due to the B_1 inhomogeneity. Since we are dealing with a sizable number of spins ($N \approx 1.06 \times 10^{10}$) inside the ensemble, the distributions of spin frequencies and couplings strengths are smooth functions around the mean values. For simplicity, we assume in our calculations that all spins couple with the mean coupling strength $g_0 = g_{\mathrm{eff}}/\sqrt{N}$ and we incorporate the inhomogeneaus broadening in a phenomenological Lorentzian spin spectral density

$$\rho(\omega) = \frac{1}{\pi\gamma_s[1 + (\frac{\omega-\omega_s}{\gamma_s})^2]}. \tag{S16}$$

This frequency distribution of spins is already sufficient to accurately describe the generation of multiple echo trains. Here γ_s is the half width at half maximum and ω_s is the mean frequency of the spin distribution.

To solve (S13)-(S15) for the inhomogeneously broadened spin ensemble, we discretize the phenomenological spin spectral density and divide the entire frequency range into $M = 40001$ equidistant frequency clusters. Each cluster k is then characterized by the mean coupling strength g_0, its detuning $\Delta_k = \omega_k - \omega_p$, and the number of spins inside this cluster. Eqs. S13-S15 can then be solved using a standard Runge-Kutta method.

Note that, along the lines of previous work [R27, R28], the distribution of coupling strengths g_k can also be included in the phenomenological spin spectral density. Calculations using such a combined spin spectral density have also been carried out and showed qualitatively similar results. In order to obtain a full quantitative agreement between our theory and the experiment, however, the exact shape of the spectral spin and spatial coupling distribution has to be determined through extensive further theoretical and experimental work [R29]. For reasons of clarity, we only present simulations in which the inhomogeneous broadening is included in the spin distribution alone, since these are already sufficient to describe the observed phenomenon of multiple echoes.

XI. A SHORT REVIEW ON MULTIPLE ECHO EFFECTS

Multiple echo effects in nuclear and electron magnetic resonance (NMR, ESR) experiments have been observed in a number of experiments, although different underlying mechanism are presented. Multiple echo signatures were reported in NMR experiments of ^{3}He, ^{3}He/^{4}He mixtures as well as water [R30–R33]. In these experiments the occurrence of multiple echos is attributed to non-linear terms in the equation of motion governing the magnetization. In Fermi liquids, the non-linearity is introduced by the Leggett-Rice effect [R32, R34]. Neither effect plays a role in our experiments. Another source for non-linear terms in the Bloch equations is the dipolar demagnetizing field [R34]. The demagnetizing field is usually negligible NMR and ESR experiments, as it is suppressed by radiation damping [R35, R36]. However, in the experiments presented in Ref. [R35, R36] a strong field gradient parallel to the static magnetic field was applied, which crucially alters the effect of the demagnetizing field on the dynamics [R36]. Another source of nonlinear spin dynamics is radiation damping [R37, R38]. Radiation damping describes the effects of a backaction of the precessing spin magnetization on the RF coil or resonator, sharing some similarities with the strong coupling regime. Numerical simulations of the nonlinear Maxwell-Bloch equations indeed show the presence of multiple echos under certain conditions [R39].

The first occurrence of a multiple echo signal in ESR was reported by Gordon and Bowers [R40]. Here, the authors conducted Hahn echo experiments of donors in silicon at a frequency of 23 GHz. We are able to estimate the relevant coupling parameters from the information supplied in the text: Assuming a typical TE_{102} cavity for operation at 23 GHz and a sample volume of $0.1\,\mathrm{cm}^3$, we estimate a filling factor of $\approx 6\,\%$. We calculate the effective coupling rate using Eq. (S3) and a donor concentration of $4\times10^{16}\,\mathrm{cm}^{-3}$ and obtain $g_{\mathrm{eff}} \approx 3.37\,\mathrm{MHz}$. With the spin relaxation rate $\gamma_s \approx 560\,\mathrm{kHz}$ and the assumption of a moderate quality factor of $Q = 200$, we estimate a cooperativity of $C = 1.68$. Therefore, the occurrence of the second echo reported in Ref. [R40] can be in hindsight explained by our model.

[R1] Stefan Weichselbaumer, Petio Natzkin, Christoph W. Zollitsch, Mathias Weiler, Rudolf Gross, and Hans Huebl, "Quantitative Modeling of Superconducting Planar Resonators for Electron Spin Resonance," Physical Review Applied **12**, 024021 (2019).

[R2] "CST Microwave Studio 2016," CST Computer Simulation Technology GmbH (2016).

[R3] J. H. Wesenberg, A. Ardavan, G. A. D. Briggs, J. J. L. Morton, R. J. Schoelkopf, D. I. Schuster, and K. Mølmer, "Quantum Computing with an Electron Spin Ensemble," Physical Review Letters **103**, 070502 (2009).

[R4] G. Feher, "Electron spin resonance experiments on donors in silicon. I. Electronic structure of donors by the electron nuclear double resonance technique," Physical Review **114**, 1219 (1959).

[R5] R. J. Schoelkopf and S. M. Girvin, "Wiring up quantum systems," Nature **451**, 664–669 (2008).

[R6] Christoph W. Zollitsch, Kai Mueller, David P. Franke, Sebastian T. B. Goennenwein, Martin S. Brandt, Rudolf Gross, and Hans Huebl, "High cooperativity coupling between a phosphorus donor spin ensemble and a superconducting microwave resonator," Applied Physics Letters **107**, 142105 (2015).

[R7] I Chiorescu, N Groll, S Bertaina, T Mori, and S Miyashita, "Magnetic strong coupling in a spin-photon system and transition to classical regime," Phys Rev B **82**, 024413 (2010).

[R8] A. Bienfait, J. J. Pla, Y. Kubo, X. Zhou, M. Stern, C. C. Lo, C. D. Weis, T. Schenkel, D. Vion, D. Esteve, J. J. L. Morton, and P. Bertet, "Controlling spin relaxation with a cavity," Nature **531**, 74–77 (2016).

[R9] J. R. Klauder and P. W. Anderson, "Spectral Diffusion Decay in Spin Resonance Experiments," Physical Review **125**, 912 (1962).

[R10] A. M. Tyryshkin, S. A. Lyon, A. V. Astashkin, and A. M. Raitsimring, "Electron spin relaxation times of phosphorus donors in silicon," Physical Review B **68**, 193207 (2003).

[R11] S. Shankar, A. M. Tyryshkin, and S. A. Lyon, "ESR measurements of phosphorus dimers in isotopically enriched ^{28}si silicon," Physical Review B **91**, 245206 (2015).

[R12] K M Salikhov, S A Dzuba, and A M Raitsimring, "The theory of electron spin-echo signal decay resulting from dipole-dipole interactions between paramagnetic centers in solids," Journal of Magnetic Resonance **42**, 255 (1981).

[R13] Alexei M Tyryshkin, Shinichi Tojo, John J L Morton, Helge Riemann, Nikolai V Abrosimov, Peter Becker, Hans-Joachim Pohl, Thomas Schenkel, Michael L W Thewalt, Kohei M Itoh, and S A Lyon, "Electron spin coherence exceeding seconds in high-purity silicon," Nature Materials **11**, 143 (2011).

[R14] D R Taylor, J R Marko, and I G Bartlet, "Exchange and Dipolar FIelds in Phosphorus-Doped Silicon Measured by Electron Spin Resonance Echoes," Solid State Commun **14**, 295 (1974).

[R15] Arthur Schweiger and Gunnar Jeschke, Principles of Pulse Electron Paramagnetic Resonance (Oxford University Press, Oxford, UK ; New York, 2001).

[R16] M.H. Alaimo and J.E. Roberts, "Effects of paramagnetic cations on the nonexponential spin-lattice relaxation of rare spin nuclei in solids," Solid State Nuclear Magnetic Resonance **8**, 241–250 (1997).

[R17] N Bloembergen, "On the interaction of nuclear spins in a crystalline lattice," Physica **15**, 386–426 (1949).

[R18] Kai W Eberhardt, Schahrazede Mouaziz, Giovanni Boero, Jürgen Brugger, and Beat H Meier, "Direct Observation of Nuclear Spin Diffusion in Real Space," Physical Review Letters **99**, 227603 (2007).

[R19] A G Redfield, "Spatial Diffusion of Spin Energy," Physical Review **116**, 315–316 (1959).

[R20] B E Vugmeister, "Spatial and Spectral Spin Diffusion in Dilute Spin Systems," physica status solidi (b) **76**, 161–170 (1976).

[R21] G Feher and E A Gere, "Electron Spin Resonance Experiments on Donors in Silicon. II. Electron Spin Relaxation Effects," Physical Review **114**, 1245 (1959).

[R22] Andrea Morello, Jarryd J Pla, Floris A Zwanenburg, Kok W Chan, Kuan Y Tan, Hans Huebl, Mikko Mottonen, Christopher D Nugroho, Changyi Yang, Jessica A van Donkelaar, Andrew D C Alves, David N Jamieson, Christopher C Escott, Lloyd C L Hollenberg, Robert G Clark, and Andrew S Dzurak, "Single-shot readout of an electron spin in silicon," Nature **467**, 687 (2010).

[R23] Hiroshi Hasegawa, "Spin-Lattice Relaxation of Shallow Donor States in Ge and Si through a Direct Phonon Process," Physical Review **118**, 1523 (1960).

[R24] M. Tavis and F.W. Cummings, "Exact Solution for an N-Molecule-Radiation-Field Hamiltonian," Physical Review **170**, 379–384 (1968).

[R25] H J Carmichael, Statistical Methods in Quantum Optics 2: Non-Classical Fields, Theoretical and Mathematical Physics (Springer Berlin Heidelberg, 2007).

[R26] M. Zens, D.O. Krimer, and S. Rotter, "Critical phenomena and nonlinear dynamics in a spin ensemble strongly coupled to a cavity. II. Semiclassical-to-quantum boundary," Physical Review A **100**, 013856 (2019).

[R27] Stefan Putz, Andreas Angerer, Dmitry O. Krimer, Ralph Glattauer, William J. Munro, Stefan Rotter, Jörg Schmiedmayer, and Johannes Majer, "Spectral hole burning and its application in microwave photonics," Nature Photonics **11**, 36 (2017).

[R28] Dmitry O. Krimer, Matthias Zens, and Stefan Rotter, "Critical phenomena and nonlinear dynamics in a spin ensemble strongly coupled to a cavity. I. Semiclassical approach," Physical Review A **100**, 013855 (2019).

[R29] K. Sandner, H. Ritsch, R. Amsüss, Ch. Koller, T. Nöbauer, S. Putz, J. Schmiedmayer, and J. Majer, "Strong magnetic coupling of an inhomogeneous nitrogen-vacancy ensemble to a cavity," Physical Review A **85**, 053806 (2012).

[R30] G. Deville, M. Bernier, and J. M. Delrieux, "NMR multiple echoes observed in solid ^{3}He," Physical Review B **19**, 5666 (1979).

[R31] G. Eska, H.-G. Willers, B. Amend, and W. Wiedemann, "Spin echo experiments in superfluid 3He," Physica B+C **108**, 1155 (1981).

[R32] D Einzel, G Eska, Y Hirayoshi, T Kopp, and P Wolfle, "Multiple Spin Echoes in a Normal Fermi Liquid," Physical Review Letters **53**, 2312 (1984).

[R33] R Bowtell, R.M Bowley, and P Glover, "Multiple spin echoes in liquids in a high magnetic field," Journal of Magnetic Resonance **88**, 643 (1990).

[R34] A. S. Bedford, R. M. Bowley, J. R. Owers-Bradley, and D. Wightman, "Multiple spin echoes in spin polarized Fermi liquids," Journal of Low Temperature Physics **85**, 389 (1991).

[R35] R. Bowtell and P. Robyr, "Structural Investigations with the Dipolar Demagnetizing Field in Solution NMR," Physical Review Letters **76**, 4971 (1996).

[R36] W.S. Warren, S. Lee, W. Richter, and S. Vathyam, "Correcting the classical dipolar demagnetizing field in solution NMR," Chemical Physics Letters **247**, 207 (1995).

[R37] Stanley Bloom, "Effects of Radiation Damping on Spin Dynamics," Journal of Applied Physics **28**, 800–805 (1957).

[R38] M.P. Augustine, "Transient properties of radiation damping," Progress in Nuclear Magnetic Resonance Spectroscopy **40**, 111–150 (2002).

[R39] A. Vlassenbroek, J. Jeener, and P. Broekaert, "Radiation damping in high resolution liquid NMR: A simulation study," The Journal of Chemical Physics **103**, 5886–5897 (1995).

[R40] J. P. Gordon and K. D. Bowers, "Microwave Spin Echoes from Donor Electrons in Silicon," Physical Review Letters **1**, 368–370 (1958).